

The rise and fall of an oxide: insights into the phase diagram of bismuth oxide on Au(111)

Alberto Turoldo,¹ Marco Bianchi,² Alessandro Baraldi,^{1, 2} and Silvano Lizzit²

¹*Dipartimento di Fisica, Università degli Studi di Trieste, 34127 Trieste, Italy*

²*Elettra-Sincrotrone Trieste, 34149 Basovizza, Italy*

(Dated: February 19, 2026)

Bismuth oxide (Bi_2O_3) is a polymorphic material of considerable technological interest, with applications spanning from heterogeneous catalysis to next-generation nanoelectronics. Despite its relevance, systematic investigations of Bi_2O_3 thin films remain scarce. Here, we report a comprehensive, multi-technique study of bismuth oxide grown on Au(111). By combining synchrotron-based x-ray photoelectron spectroscopy and diffraction with low-energy electron diffraction and scanning tunneling microscopy, we elucidate the structural evolution of the surface during controlled oxidation and subsequent annealing. We find that Bi deposition induces well-defined surface reconstructions, whereas oxidation triggers the formation of a complex sequence of Bi_2O_3 domains. High-resolution spectroscopic and diffraction data enable us to propose a structural model consistent with the (201) surface of $\beta\text{-Bi}_2\text{O}_3$. In addition, work function measurements reveal substantial electronic modifications at the interface. These results provide benchmark structural and electronic insights into the Bi oxide/Au(111) system and establish a framework for integrating Bi_2O_3 in devices in combination to two-dimensional semiconductors exploiting its low contact resistance.

I. INTRODUCTION

Bismuth forms several oxides with distinct stoichiometries and crystal structures, among which Bi_2O_3 is the most stable and extensively investigated phase. This is a polymorphic material of considerable technological relevance, exhibiting a wide range of functional properties that have been extensively explored over the past decades^{1–7}. Its applications extend from resistive components⁸ and heterogeneous catalysis^{9,10} to visible-light photocatalysis^{11–13} and, more recently, to p-type semiconducting channels for nanoscale transistors¹⁴. Of particular interest is its potential use as an interfacial layer to reduce Schottky barriers in contact to transition-metal dichalcogenides (TMDs)^{15,16}. More generally, two-dimensional (2D) dielectric nanosheets represent a versatile platform when integrated with other 2D materials such as graphene. A notable example is the formation of graphene– Al_2O_3 nanosheet interfaces, where an ultra-thin alumina layer enables electronic decoupling while preserving structural integrity¹⁷.

Despite this broad technological interest, a detailed understanding of the growth and oxidation of Bi thin films under well-controlled ultra-high vacuum (UHV) conditions remains incomplete. Recent reports indicate that Bi-based contacts can suppress metal-induced gap states at TMD interfaces^{15,18}, underscoring the need for a systematic characterization of the structural and electronic properties of Bi and its oxides at metal surfaces. However, comprehensive surface-science studies of Bi oxide formation on Au(111)—which is widely used as supporting substrate for two-dimensional materials—are still lacking.

In this work, we address this gap through a multi-technique investigation of Bi oxide growth on Au(111), combining synchrotron-based structural and spectro-

scopic probes with diffraction and microscopy techniques to resolve the evolution of the interface under controlled preparation conditions.

II. EXPERIMENTAL METHODS

Experiments were carried out at the SuperESCA beamline of Elettra Sincrotrone Trieste¹⁹ (IT), including its CoSMoS branch line equipped with a monochromatized $\text{Al K}\alpha$ x-ray source, and at the SGM3 beamline of ASTRID2 (DK).

Surface characterization combined complementary imaging, diffraction and spectroscopic techniques. X-ray photoemission spectroscopy (XPS) was employed in all laboratories as key tool to determine chemical composition and oxidation states²⁰, while x-ray photoelectron diffraction (XPD) performed on the SuperESCA beamline provided local structural information. Long-range surface order was assessed by low energy electron diffraction (LEED) at all the facilities, and real-space morphology was investigated by scanning tunnelling microscopy (STM) on CoSMoS and SGM3.

Clean Au(111) surfaces were prepared by repeated cycles of Ar^+ sputtering and annealing up to 970 K. Surface cleanliness and long-range order were verified by XPS, LEED, and STM. Bismuth was deposited onto Au(111) under ultra-high vacuum (UHV) conditions from a home-built evaporator, with the substrate maintained at approximately 373 K. The temperature was monitored using a K-type thermocouple in direct contact with the crystal. The chemical purity of the deposited Bi and the absence of contaminants were confirmed by XPS. Oxidation was performed by exposing the Bi-covered surface to high-purity O_2 through a home made doser positioned close to the sample, enabling a local pressure up to 10^{-3} mbar while maintaining a chamber pressure

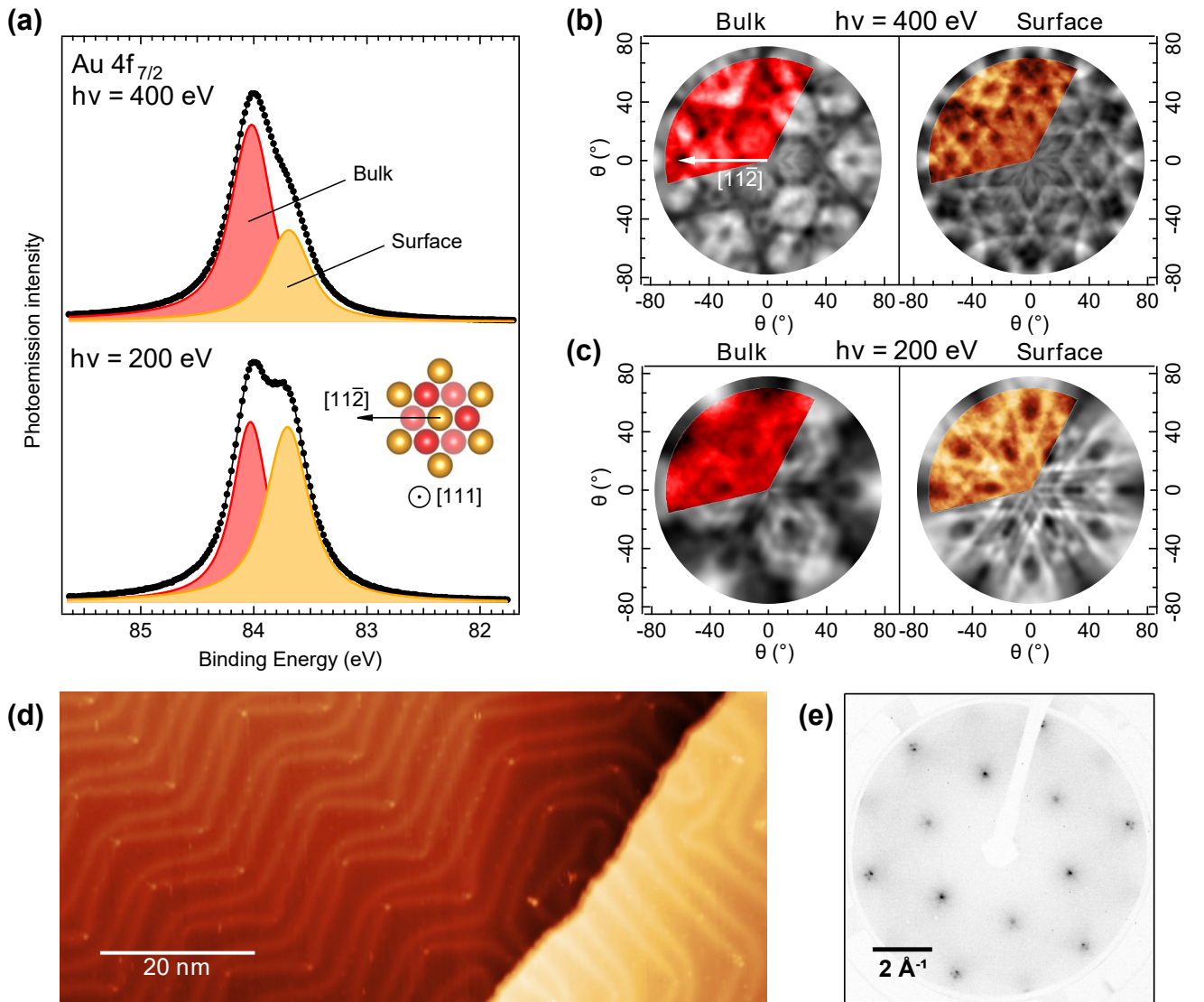


FIG. 1: Characterization of the Au(111) surface. (a) Au 4f_{7/2} core level spectrum acquired at photon energies $h\nu = 400$ and 200 eV. Acquired data are displayed as points while fitted bulk and surface components in solid areas. The atomic model of the surface is presented. (b)-(c) Stereographic projection of the modulation function χ for the bulk and surface components acquired at $h\nu = 400$ eV and $h\nu = 200$ eV (corresponding to a kinetic energy of 316 and 116 eV, respectively). Acquired data (colored section) is compared with XPD simulation (greyscale) and the $[11\bar{2}]$ direction is indicated as reference. (d) STM image displaying the herringbone reconstruction of the Au(111) surface ($I = 0.40$ nA, $V = 1.60$ V), with low coverage of Bi visible as faint bright protrusions on the herringbone elbows. (e) LEED pattern obtained at $E_k = 137$ eV, the herringbone reconstruction generates the additional spots surrounding the first order Au(111) diffraction peaks.

of 10^{-5} mbar, similarly to what has been done in other works²¹. Oxidation at higher pressures was performed in a dedicated gass-cell connected to the UHV chambers.

XPS measurements were performed at room temperature with Normal Emission geometry (unless otherwise specified) using synchrotron radiation and a Phoibos 150 analyzer, achieving a combined energy resolution better than 50 meV. All the spectra are shown after subtraction of a linear background and calibration of the Binding Energy (BE) with respect to the measured Fermi Level E_F . The work function Φ was determined from photoemission

measurements²² by determining E_F^{kin} , and the secondary-electron cutoff, $E_{\text{tail}}^{\text{kin}}$, according to the equation

$$\Phi = h\nu - (E_F^{\text{kin}} - E_{\text{tail}}^{\text{kin}}). \quad (1)$$

A small bias voltage was applied to the sample during these measurements. All the spectra acquired for the secondary electron cutoff identification employed photon energies of 109.95 eV or 145.05 eV.

XPD data are presented as stereographic projections of the modulation function χ , defined as in Ref. ²³. Experimental patterns (χ_{exp}) were compared with multiple-

scattering simulations (χ_{sim}) based on trial atomic configurations generated using the Electron Diffraction in Atomic Clusters (EDAC) package²⁴. Starting crystallographic parameters were obtained from the Materials Cloud²⁵. Agreement between simulated and experimental patterns is quantified in terms of the R-factor²⁶ defined as

$$R = \frac{\sum_i (\chi_{i,exp} - \chi_{i,sim})^2}{\sum_i (\chi_{i,exp}^2 + \chi_{i,sim}^2)}. \quad (2)$$

LEED kinematic simulations were performed with Pro-LEED Studio²⁷. Consistency of the preparations in the different laboratories was ensured by comparing core level spectra, LEED patterns and STM images.

STM topographs were acquired at room temperature (RT) using Aarhus STMs equipped with a PtIr tip. Image processing and analysis were performed with the WSxM software package²⁸ while structural models were visualized using the VESTA software²⁹.

III. RESULTS AND DISCUSSION

A. Bi adsorption on Au(111)

Figure 1 shows reference data for clean Au(111). LEED and STM confirm the herringbone reconstruction^{30,31}. The Au $4f_{7/2}$ spectrum exhibits a surface core-level shift of 0.32 eV, consistent with literature values^{32,33}. XPD patterns of the surface and bulk components reproduce the expected symmetry: nearly six-fold for the surface layer and three-fold for the bulk, as dictated by the Au(111) termination^{32,34}. The bulk component is used to determine the reference for crystallographic orientation.

Figure 2 summarizes the structural evolution upon increasing Bi coverage. At submonolayer regime, the $(\sqrt{37} \times \sqrt{37})$ reconstruction is observed, while for increasing Bi depositions a $(P \times \sqrt{3})$ phase appears, where $P = 5, 8, 11, 14$ respectively for increasing coverages describes the moiré cell size with respect to the underlying Au, in agreement with previous reports^{35–38}. LEED and STM confirm the high degree of order across the explored thickness range. Bi $4f_{7/2}$ spectra confirm cleanliness of the deposition method showing a single component at a $BE = 156.9$ eV in the multilayer regime, consistent with values found in literature⁷.

As reported in literature^{36–38}, increasing the Bi thickness leads to a progressive evolution toward a bulk-like Bi(110) termination, with the in-plane lattice aligned along the $[11\bar{2}]$ and $[1\bar{1}0]$ directions of the substrate. The XPD data confirm this trend in the multilayer regime (Fig. 2(f)), showing qualitative agreement with simulations based on a bulk terminated Bi(110) structural model comprising six symmetry-related domains (three rotational variants and their mirror counterparts). However, the resulting R-factor values are not fully satisfac-

tory. In particular, for the pattern acquired at low kinetic energy (backscattering regime) we obtain $R = 0.43$, while in the forward-scattering regime the agreement further deteriorates, reaching $R = 0.7$. Such behaviour is not unexpected and can be rationalized in terms of the complex structure of the thick Bi overlayer described in Ref.³⁸ together with a sensitivity to deeper layers that increases with increasing kinetic energy. According to Ref.^{39,40}, growth proceeds via weakly interacting bilayers stacked on a saturated interfacial Bi layer, as expected for the (110) termination. Away from the Au interface, the semi-layered Bi structure progressively relaxes from the $(P \times \sqrt{3})$ interfacial arrangement toward the bulk-like (110) as the film thickness increases. In addition to this, in the multilayer regime, the area probed by photoemission includes zones with different thicknesses, all contributing incoherently to the measured patterns. Such complex stacking, extensively described in the literature, differs from the simplified bulk model used in this work. Although additional buckling was introduced into the bulk-like Bi(110) structural model in an attempt to refine the agreement, this did not lead to any significant improvement. A systematic search for a more realistic model for this well known system is however out of the scope of this work.

B. Oxidation pathway of Bi films

Room temperature oxidation of a 3-5 ML Bi film at a background pressure of 10^{-6} mbar induces the gradual emergence of Bi^{3+} components in the Bi $4f$ spectrum (Fig. 4(a)).

More efficient oxidation is achieved using a doser providing a local O_2 pressure of 10^{-3} mbar on the surface (Fig. 4(b)) and leading to the clear appearance of the oxide peak at $BE = 158.6$ eV. STM reveals the formation of nanoscale oxide domains with different orientations (Fig. 3). Oxidation at such high pressure but at a moderate temperature of 423 K leads to the complete disappearance of the metallic Bi and shift of the oxide peak to 158.8 eV, (blue line in Fig. 4(b)), indicating full conversion to Bi^{3+} , consistent with literature values^{10,12,41}.

In particular, the total intensity of Bi $4f_{7/2}$ photoemission (metallic + oxidized components) increases by up to a factor of 2.5 compared to the film deposited. Such effect cannot be explained by the difference in electron mean free path inside the newly formed Bi_2O_3 layer, nor by diffraction, that shows only weak modulation in the photoemission intensity as a function of photoemission angle. This behaviour could be explained if an initial 3D multilayer system transforms, upon oxidation, into a quasi-2D structure, where emitters that were previously screened by the overlayers become exposed as the system evolves toward a two-dimensional configuration. However our STM observations, consistent with Vincente *et al.*³⁸, clearly show that our initial Bi surface, even in the high coverage regime, is regularly flat and ordered as ex-

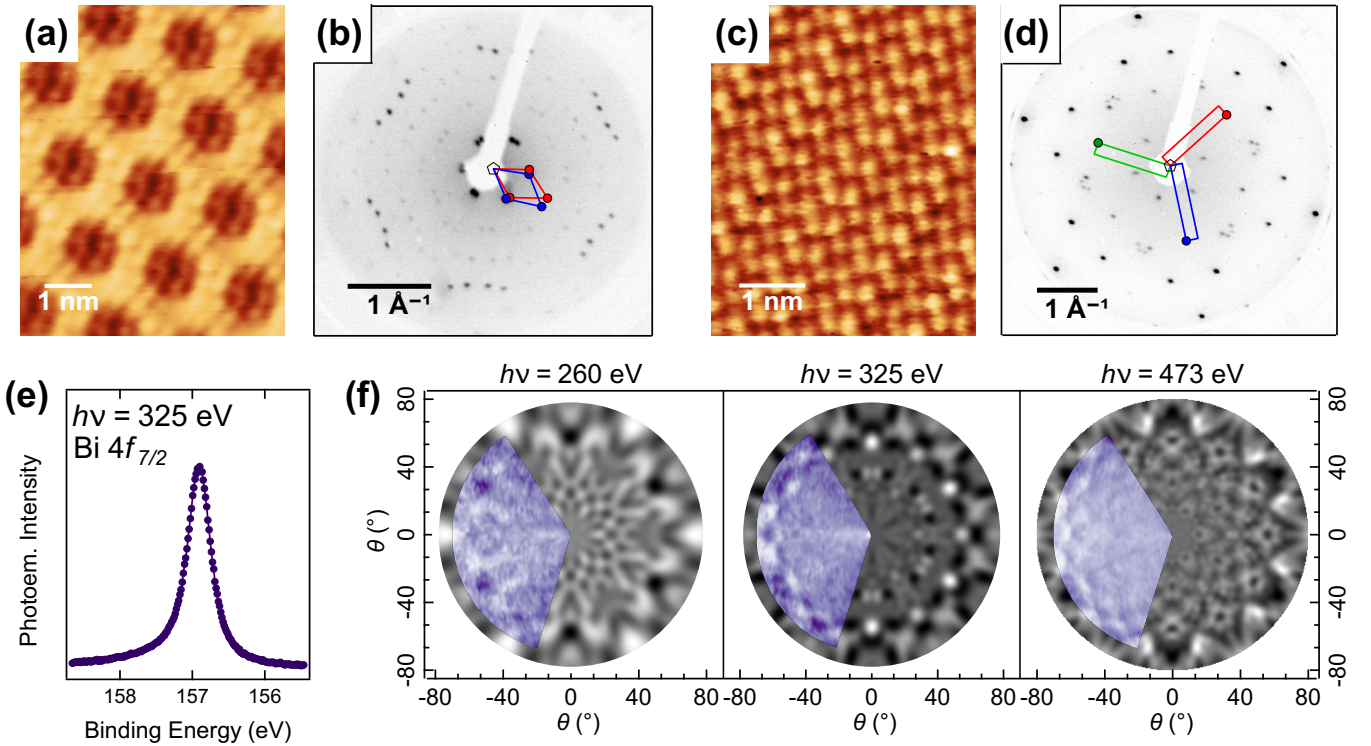


FIG. 2: Phases for Bi deposition on Au(111). (a)-(b) $(\sqrt{37} \times \sqrt{37}) R25.3^\circ$ phase. (a) STM image displaying honeycomb structure ($I = 0.22$ nA, $V = 0.23$ V); (b) LEED image acquired at $E_k = 38$ eV with highlighted unit cells (red/blue) associated to different rotational domains. (c)-(d) $(P \times \sqrt{3})$ phase, with $P = 11$. (c) STM image showing striped pattern associated to the moiré supercells ($I = 0.12$ nA, $V = 1.95$ V); (d) LEED image acquired at $E_k = 38$ eV with highlighted unit cells (red/green/blue) associated to different rotational domains. (e) High resolution Bi $4f_{7/2}$ core level spectrum obtained after bismuth deposition in the multilayer regime, acquired at $h\nu = 325$ eV. (f) Stereographic projections of the modulation function χ of the Bi $4f_{7/2}$ peak at different kinetic energies; The acquired data (colored section) are compared with XPD simulations (greyscale).

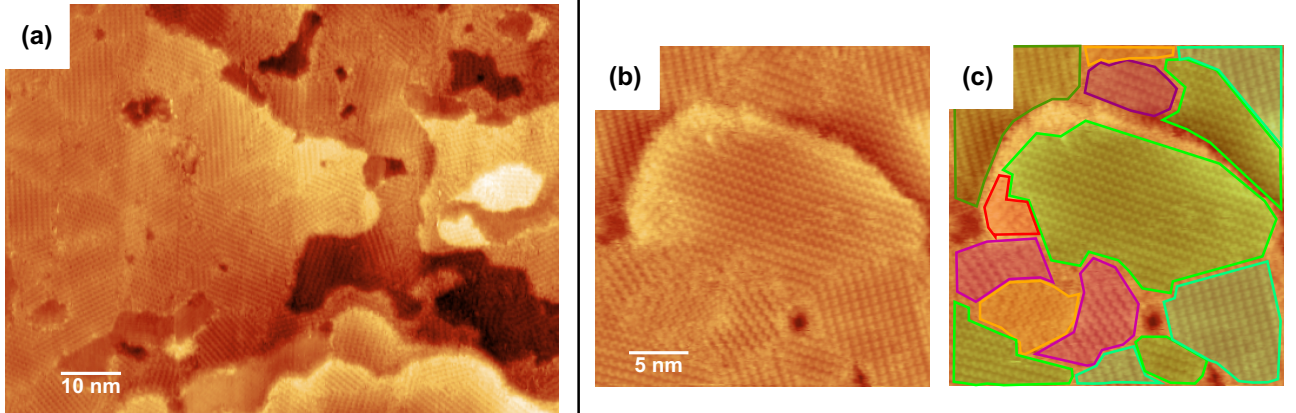


FIG. 3: STM images of the thin layer of bismuth (3-5 ML) on Au(111) after RT oxidation. (a) A large scale view of the surface, displaying ordered oxide nanoscale domains ($I = 0.16$ nA, $V = 0.98$ V). (b)-(c) The domains on the surface are highlighted with different colors based on the electronic contrast produced ($I = 0.22$ nA, $V = 1.32$ V).

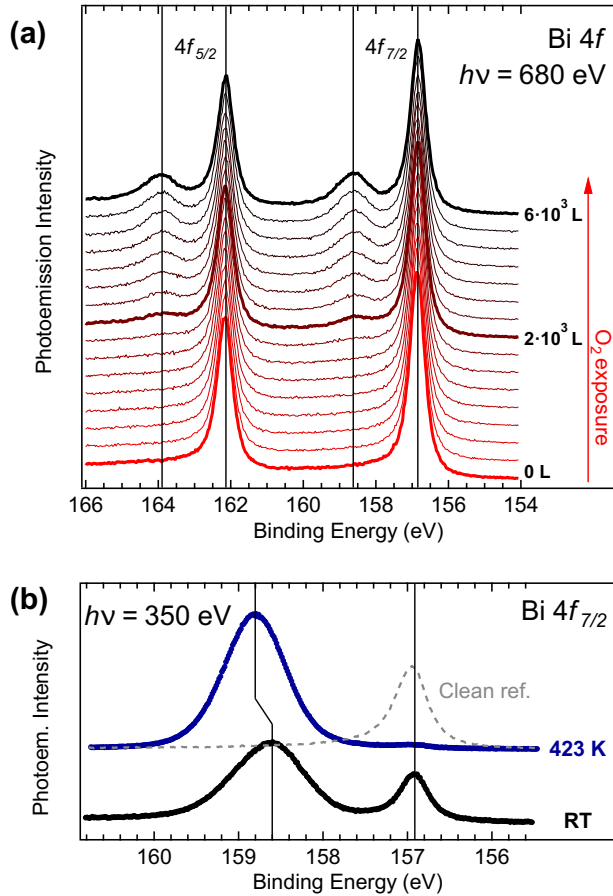


FIG. 4: (a) Bi 4f core level spectra after increasing exposure of Bi/Au(111) to O₂ at RT. New components emerge at higher BE that are associated with oxidized Bi⁺³ species. (b) High resolution Bi 4f_{7/2} core level spectra obtained after oxidation at different temperatures, with reference before oxidation. Oxidation at 423 K leads to the almost complete disappearance of the component related to metallic Bi.

pected for metal surfaces. We explain such effect based on two observations: the density of Bi atoms in the oxide matrix is expected to be lower than the one in the metal, leading to a layer thickness that after oxidation is greater than the pristine one, together with a mechanism of surface segregation of Bi atoms from the bulk Au during oxidation, consistently with the known behaviour for metals in Au host crystals upon oxidation explained by Berti *et al.*⁴².

LEED patterns acquired after oxidation at different temperatures (Fig. 6) display numerous faint diffraction spots, consistent with the small oxide domains observed by STM. Despite this complexity, twelve bright spots at $k_{\parallel} \approx 1.78 \text{ \AA}^{-1}$ are systematically observed for oxidation up to 423 K, with only minor variations in their angular separation 2α (Fig. 6(g)). The persistence of these features indicates only a partial long-range order, consistently with what is observed in STM. Radial position and symmetry of the LEED spots are compatible

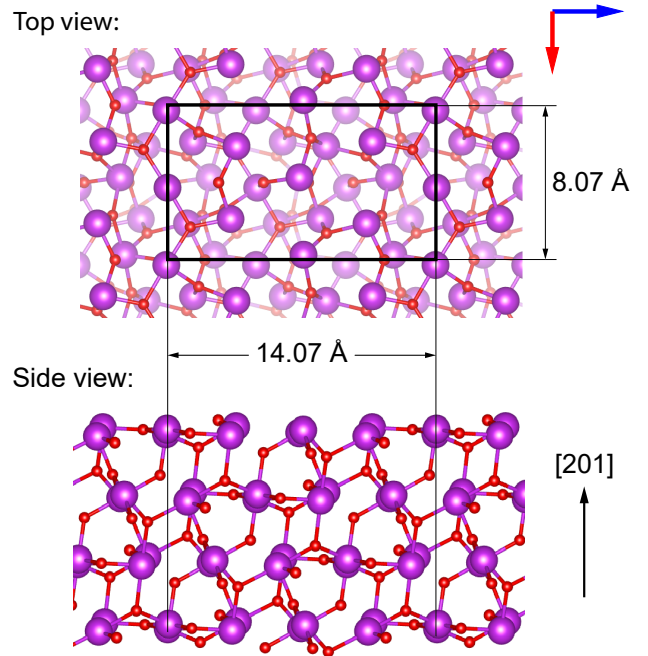


FIG. 5: Atomic model of the β -Bi₂O₃(201) termination employed for XPD simulation; Purple - Bi, Red - O.. Colored arrows represent inequivalent directions in the top view of the atomic model here as well as in the diffraction pattern shown in Fig. 7(a).

with the (201) surface termination of β -Bi₂O₃, already observed in previous reports^{12,43,44}. In particular, the twelve diffraction spots at $\approx 1.78 \text{ \AA}^{-1}$ can be rationalized by rotational and/or mirror domains of the (201) surface, comprising unit cells rotated by $\pm\alpha$ relative to the [112] directions of the three-fold Au(111) substrate.

Such interpretation is consistent with the XPD results presented in Fig. 7. At low kinetic energy ($E_k \approx 100 \text{ eV}$), corresponding to a backward-scattering regime, no pronounced diffraction features are resolved. This is attributed to the coexistence of multiple ordered domains, as evidenced by LEED and STM, and their various azimuthal orientations. However, in more bulk-sensitive forward-scattering regime, i.e. by employing higher photon energies, allowing for higher kinetic energy electrons ($E_k = 491 \text{ eV}$), the acquired pattern shows clearly defined features.

Data acquired after oxidation at 423 K are also consistent with the β -Bi₂O₃(201) termination as a recurring local structural motif. Fig. 5 shows the structural model used for the simulations of the diffraction patterns: those include emitters from the first three Bi layers, while deeper layers do not significantly affect the pattern (R-factor variation $\lesssim 0.01$ upon inclusion).

An accurate reproduction of the experimental data is obtained by considering at least twelve symmetry-equivalent domains and optimizing the rotation angle α as suggested by LEED, yielding a minimum R-factor of

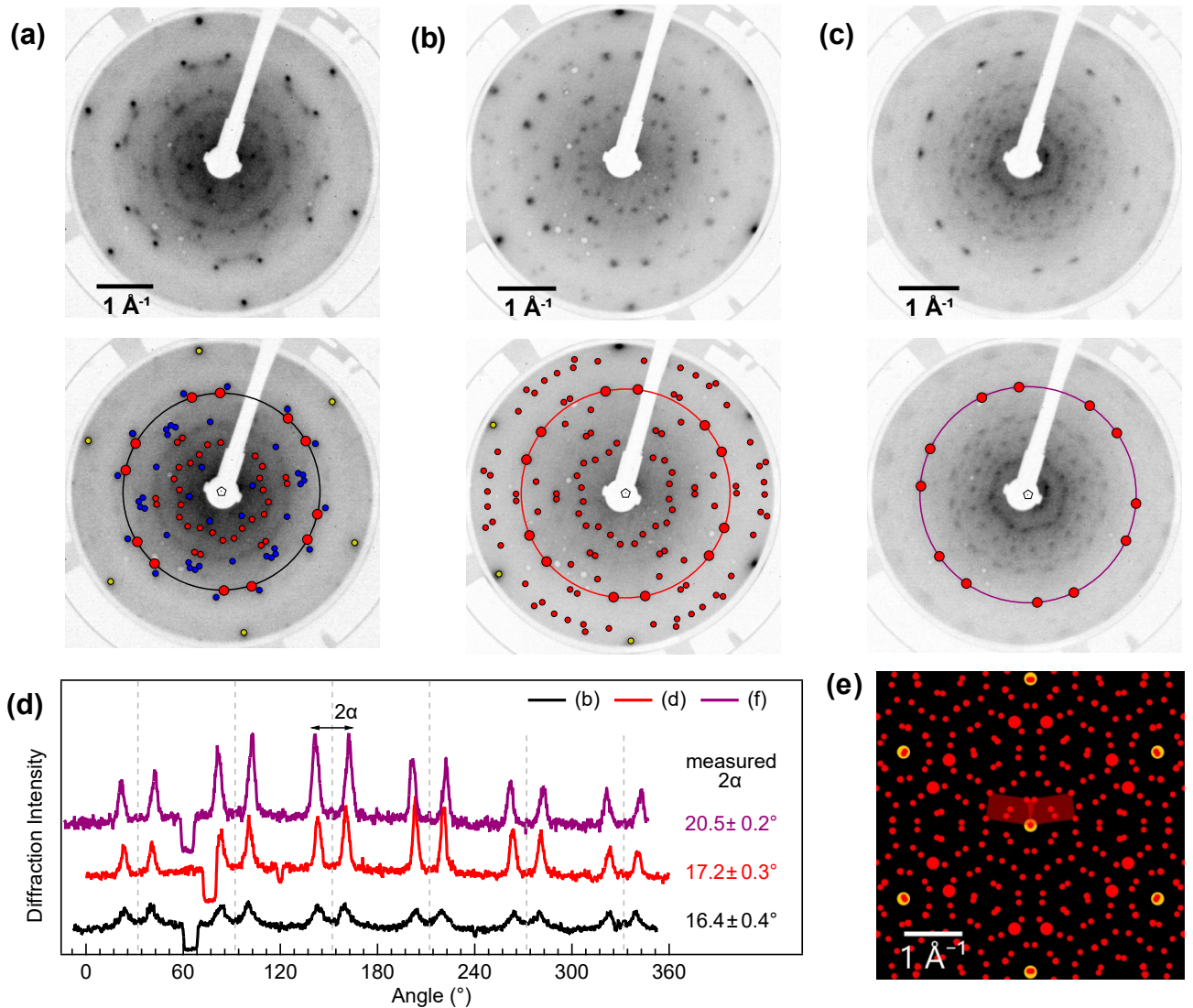


FIG. 6: LEED diffraction patterns obtained at $E_k = 38$ eV after oxidation of the bismuth layer under different conditions. Images at the top are superimposed to the simulations at the bottom^b. (a) Oxidation at RT (corresponding to the spectrum in Fig. 4). (b) Cycles of Bi evaporation and Bi oxidation at a pressure of 1 mbar. (c) Oxidation at 423 K (see spectrum in Fig. 4). Discrepancies in azimuthal orientation between (a)-(c) and (b) are due to remounting of the sample with respect to the LEED optics. The highlighted diffraction spots are associated to: yellow - Au(111) substrate; blue - $(P \times \sqrt{3})$ phase for metallic Bi on Au(111); red - bismuth oxide. (d) Circular line profiles with radius $\approx 1.78 \text{ \AA}^{-1}$ extracted from (a)-(b)-(c) along the circles with corresponding colors. (e) Simulated diffraction pattern obtained using the kinematic theory and a matrix $\begin{pmatrix} 3.01 & 0.48 \\ 2.06 & 5.58 \end{pmatrix}$ corresponding to the (201) termination of $\beta\text{-Bi}_2\text{O}_3$ for the case $2\alpha = 17.2^\circ$ two differently oriented unit cells are highlighted in red for clarity.

$R = 0.20$. Restricting the model to the two coupled domains rotated by $\pm\alpha$ with respect to the $[11\bar{2}]$ direction and their threefold symmetric equivalents results in a significantly poorer agreement ($R = 0.48$). Inclusion of additional mirrored (equivalently, 180° -rotated) domains substantially improves the agreement and reproduces the experimental pattern (Fig. 7). Following an approach analogous to the Pendry analysis of LEED I-V curves⁴⁵, the uncertainty in the minimum R-factor R_m can be estimated as $\Delta R_m = \sqrt{2/N_p} R_m$, where N_p is the num-

ber of well-separated diffraction features. Estimating N_p from the azimuthal XPD scans at different polar emission angles^{32,34} gives $\Delta R_m = 0.015$. This constrains the angular separation to $2\alpha = 20.7 \pm 3.0^\circ$, in agreement with the LEED analysis for the oxide prepared at the same temperature.

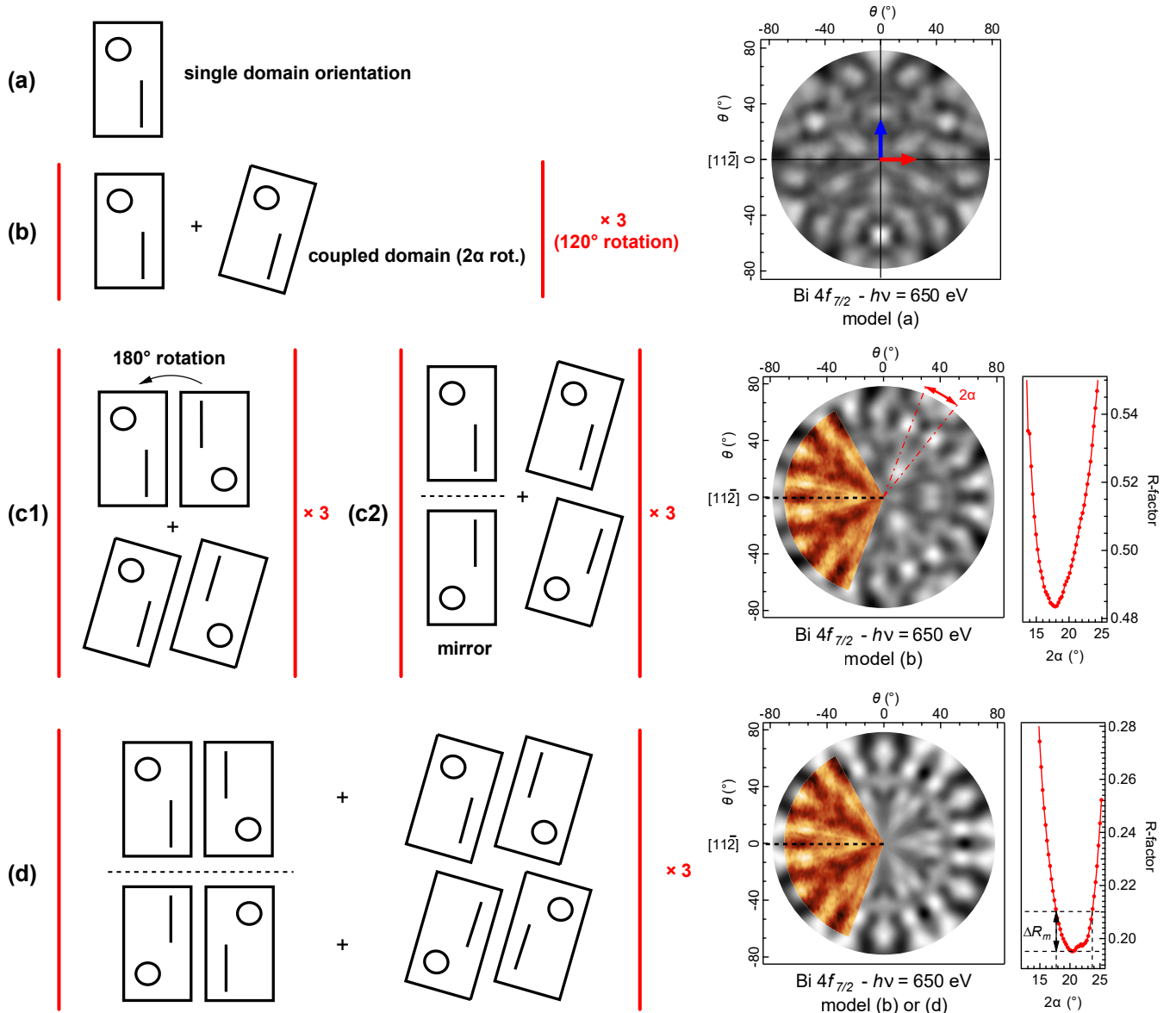


FIG. 7: Left: models depicting possible combinations of β -Bi₂O₃(201) domains on the surface, including the presence of coupled domains with a reciprocal rotation of 2α as evidenced in LEED (Fig. 6). Right: simulated diffraction pattern associated with a model (greyscale) is compared with the experimental data (colored section) for Bi 4f_{7/2} emission at $h\nu = 650$ eV ($E_k = 491$ eV); the R-factor dependence on the value of the separation angle 2α is shown on the right. (a) Model for a single orientation of β -Bi₂O₃(201) with corresponding simulated diffraction pattern. Colored arrows represent inequivalent directions in the top view of the atomic model presented in Fig. 5. While model (b), consisting of 6 unique domains, gives $R_m = 0.48$, models (c) or (d), with 12 or 24 unique domains, equivalently produce a significantly improved agreement with the experimental data with $R_m = 0.20$. The confidence interval for the value R_m is reported.

C. High-temperature restructuring

Temperature-dependent XPS measurements performed in UHV on samples oxidized at RT (Fig. 8) reveal a non-monotonic evolution. Upon annealing, a loss of oxidized Bi spectral weight is observed, accompanied by the reappearance of same metallic Bi at 810 K. Surprisingly, when reaching temperatures above 870 K and without supplying any O₂, complete

oxidation is observed together with clear evidence of bulk incorporation. The Bi³⁺ component becomes the predominant one and appears at a slightly lower BE than the pristine oxide ($BE = 158.4$ eV). STM images corroborate this, showing the formation of disordered regions and domains with symmetry distinct from that present prior to annealing, indicative of a restructuring of the oxide layer (Fig. 9).

Oxidation performed directly at 500 K yields an even

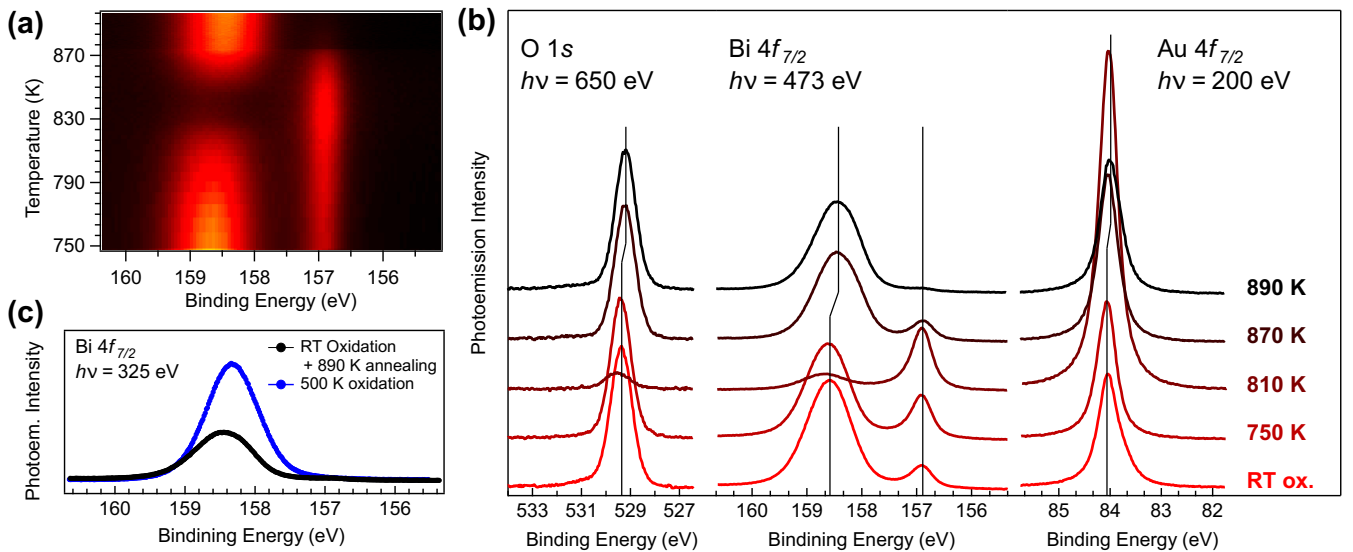


FIG. 8: XPS evidence of the complex restructuring sequence following annealing of the bismuth oxide layer prepared with RT oxidation. (a) Temperature resolved spectra of the Bi 4f_{7/2} core level acquired at $h\nu = 325$ eV, displaying significant peak modulation due to surface reordering. The obtained figure is a result of stitching subsequent temperature ramps up to an increasing maximum temperature of 890 K. (b) High resolution spectra for O 1s ($h\nu = 650$ eV), Bi 4f_{7/2} ($h\nu = 473$ eV) and Au 4f_{7/2} ($h\nu = 200$ eV) core levels at different steps of the annealing ramp. Each spectrum was acquired after the sample had cooled down to RT. (c) High resolution Bi 4f_{7/2} core level spectra comparison after the annealing ramp and after 500 K oxidation of the deposited Bi layer.

lower BE value ($BE = 158.3$ eV). This convergence indicates that annealing of the RT-prepared oxide drives the system toward a very similar chemical state achieved by direct high-temperature (500 K) oxidation. This sequence is not observed for samples oxidized directly at elevated temperature ($\gtrsim 500$ K). As shown in Fig. 8(c), the Bi 4f_{7/2} peak after annealing to 890 K (following RT oxidation) appears at 158.4 eV, shifted by ~ 150 meV with respect to the one obtained for direct oxidation at 500 K.

Such complex evolution can be rationalized as follows. For $T \lesssim 830$ K, oxygen redistributes from the near-surface region throughout the Bi film. The concomitant decrease in Bi 4f oxide-component and O 1s intensity, together with the increase in metallic Bi and Au signals, is consistent with Au surface segregation, likely filling vacancies generated by oxygen redistribution upon annealing. At higher temperature, the system undergoes a structural transformation toward a more stable Bi₂O₃ polymorph. In this regime, oxide formation becomes energetically favored over Au–Bi alloying at the surface, leading to a renewed increase in oxidized Bi and O intensity and a corresponding suppression of metallic Bi and Au contributions.

D. Electronic structure

Work function measurements (Table I) show a substantial decrease upon oxidation: from 4.1 eV (Bi/Au(111))

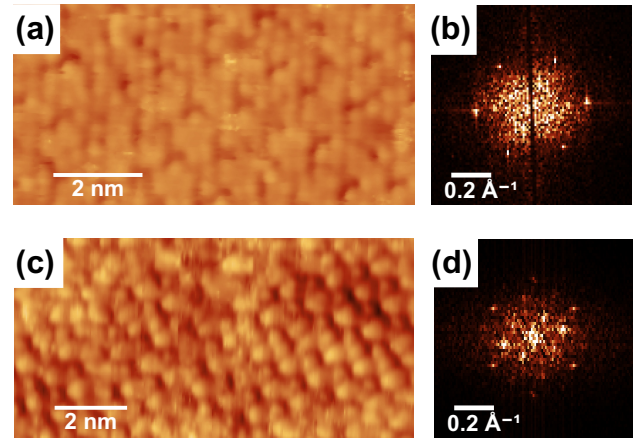


FIG. 9: STM images of oxide nanoscale disordered domains that appear following the reordering process displayed in Fig. 8. (a) $I = 0.14$ nA, $V = 1.57$ V; (b) Corresponding FFT. (c) $I = 0.10$ nA, $V = 0.44$; (d) corresponding FFT.

to ~ 3.6 eV (depending on the preparation of Bi₂O₃/Au(111)). This shift reflects significant changes in surface dipole and electronic structure, underlining the potential of Bi oxides for tuning Schottky barriers in contact engineering.

Surface	Preparation	Φ (eV)
Au(111)	clean	5.4
Bi/Au(111)	3-5 ML coverage	4.1
Bi ₂ O ₃ /Au(111)	503 K oxidation	3.8
	+ annealing 673 K	3.6
	+ annealing 923 K C	3.5
Bi ₂ O ₃ /Au(111)	423 K oxidation	3.4

TABLE I: Experimentally measured work functions.

IV. CONCLUSIONS AND OUTLOOK

We have provided a systematic study of Bi₂O₃ thin films grown on Au(111) based on complementary techniques. The analysis reveals a complex oxidation pathway leading to multiple Bi oxide structures on the motives consistent with the (201) surface of β -Bi₂O₃ appearing with at least 12 domains. Annealing induces a complex restructuring mechanism involving diffusion of Au to the surface and possibly rearrangements of oxygen

vacancies.

Beyond the structural models proposed here, our work highlights several promising directions. First, the ability to tune the Bi oxide surface termination by controlled oxidation and annealing could be exploited to engineer specific interface properties. Second, the observed work function decrease upon oxidation indicates potential for tailoring Schottky barriers when the layer is put in contacts to semiconductors, e.g. transition-metal dichalcogenides.

Acknowledgments

We acknowledge support from the staff of Elettra-Sincrotrone Trieste. Discussions with Philip Hofmann from Aarhus University (DK) were highly valuable. A.B. acknowledges the financial support from the National Quantum Science and Technology Institute (PNRR MUR project-PE0000023-NQSTI). A.T. acknowledges support from Collegio Universitario "Luciano Fonda".

¹ W. Guertler, Zeitschrift für anorganische Chemie **37**, 222 (1903).

² G. Gattow and D. Schütze, Zeitschrift für anorganische und allgemeine Chemie **328**, 44 (1964).

³ C. N. R. Rao, G. V. S. Rao, and S. Ramdas, The Journal of Physical Chemistry **73**, 672 (1969).

⁴ H. Harwig and A. Gerards, Thermochimica Acta **28**, 121 (1979).

⁵ A. F. Gualtieri, S. Immovilli, and M. Prudenziati, Powder Diffraction **12**, 90 (1997).

⁶ N. Cornei, N. Tancret, F. Abraham, and O. Mentré, Inorganic Chemistry **45**, 4886 (2006).

⁷ M. Drache, P. Roussel, and J.-P. Wignacourt, Chemical Reviews **107**, 80 (2007).

⁸ T. Maeder, International Materials Reviews **58**, 3 (2013).

⁹ Y. Lou, L. Wang, Z. Zhao, Y. Zhang, Z. Zhang, G. Lu, Y. Guo, and Y. Guo, Applied Catalysis B: Environmental **146**, 43 (2014).

¹⁰ J. Chen, C. Wang, C. Zong, S. Chen, P. Wang, and Q. Chen, ACS Applied Materials & Interfaces **13**, 29532 (2021).

¹¹ X. Xiao, R. Hu, C. Liu, C. Xing, C. Qian, X. Zuo, J. Nan, and L. Wang, Applied Catalysis B: Environmental **140**–**141**, 433 (2013).

¹² S. Tian, I. A. Bello, J. Peng, H. Ren, Q. Ma, M. Zhu, K. Li, H. Wang, J. Wu, and G. Zhu, Journal of Alloys and Compounds **854**, 157223 (2021).

¹³ E. Hashemi, R. Poursalehi, and H. Delavari, Journal of Science: Advanced Materials and Devices **10**, 100834 (2025).

¹⁴ Y. Xiong, D. Xu, Y. Zou, L. Xu, Y. Yan, J. Wu, C. Qian, X. Song, K. Qu, T. Zhao, J. Gao, J. Yang, K. Zhang, S. Zhang, P. Wang, X. Chen, and H. Zeng, Nature Materials **24**, 688 (2025).

¹⁵ P.-C. Shen, C. Su, Y. Lin, A.-S. Chou, C.-C. Cheng, J.-H. Park, M.-H. Chiu, A.-Y. Lu, H.-L. Tang, M. M. Tavakoli, G. Pitner, X. Ji, Z. Cai, N. Mao, J. Wang, V. Tung, J. Li, J. Bokor, A. Zettl, C.-I. Wu, T. Palacios, L.-J. Li, and J. Kong, Nature **593**, 211 (2021).

¹⁶ W. Li, X. Gong, Z. Yu, L. Ma, W. Sun, S. Gao, Ç. Köroğlu, W. Wang, L. Liu, T. Li, H. Ning, D. Fan, Y. Xu, X. Tu, T. Xu, L. Sun, W. Wang, J. Lu, Z. Ni, J. Li, X. Duan, P. Wang, Y. Nie, H. Qiu, Y. Shi, E. Pop, J. Wang, and X. Wang, Nature **613**, 274 (2023).

¹⁷ L. Omiciuolo, E. R. Hernández, E. Miniussi, F. Orlando, P. Lacovig, S. Lizzit, T. O. Menteş, A. Locatelli, R. Larciprete, M. Bianchi, S. Ulstrup, P. Hofmann, D. Alfè, and A. Baraldi, Nature Communications **5**, 5062 (2014).

¹⁸ T. Su, Y. Li, Q. Wang, W. Zhao, L. Cao, and Y. S. Ang, Journal of Physics D: Applied Physics **56**, 234001 (2023).

¹⁹ A. Abrami, M. Barnaba, L. Battistello, A. Bianco, B. Brena, G. Cautero, Q. H. Chen, D. Cocco, G. Comelli, S. Contrino, F. De Bona, S. Di Fonzo, C. Fava, P. Finetti, P. Furlan, A. Galimberti, A. Gambitta, D. Giuretti, R. Godnig, W. Jark, S. Lizzit, F. Mazzolini, P. Melpignano, L. Olivi, G. Paolucci, R. Pugliese, S. N. Qian, R. Rosei, G. Sandrin, A. Savoia, R. Sergio, G. Sostero, R. Tommasini, M. Tudor, D. Vivoda, F.-Q. Wei, and F. Zanini, Review of Scientific Instruments **66**, 1618 (1995).

²⁰ L. Bignardi, P. Lacovig, R. Larciprete, D. Alfè, S. Lizzit, and A. Baraldi, Surface Science Reports **78**, 100586 (2023).

²¹ S. Lizzit, R. Larciprete, P. Lacovig, M. Dalmiglio, F. Orlando, A. Baraldi, L. Gammelgaard, L. Barreto, M. Bianchi, E. Perkins, and P. Hofmann, Nano Letters **12**, 4503 (2012).

²² A. P. Baddorf, Scientific Reports **13**, 10.1038/s41598-023-40187-5 (2023).

²³ F. Orlando, P. Lacovig, L. Omiciuolo, N. G. Apostol, R. Larciprete, A. Baraldi, and S. Lizzit, ACS Nano **8**, 12063 (2014).

²⁴ F. J. García de Abajo, M. A. Van Hove, and C. S. Fadley, Physical Review B **63**, 075404 (2001).

²⁵ L. Talirz, S. Kumbhar, E. Passaro, A. V. Yakutovich,

V. Granata, F. Gargiulo, M. Borelli, M. Uhrin, S. P. Huber, S. Zoupanos, C. S. Adorf, C. W. Andersen, O. Schütt, C. A. Pignedoli, D. Passerone, J. VandeVondele, T. C. Schulthess, B. Smit, G. Pizzi, and N. Marzari, *Sci. Data* **7**, 299 (2020).

²⁶ D. Woodruff, *Surface Science Reports* **62**, 1 (2007).

²⁷ P. Procházka and J. Čechal, *Journal of Applied Crystallography* **57**, 187 (2024).

²⁸ I. Horcas, R. Fernández, J. M. Gómez-Rodríguez, J. Colchero, J. Gómez-Herrero, and A. M. Baro, *Review of Scientific Instruments* **78**, 013705 (2007).

²⁹ K. Momma and F. Izumi, *Journal of Applied Crystallography* **44**, 1272 (2011).

³⁰ J. V. Barth, H. Brune, G. Ertl, and R. J. Behm, *Physical Review B* **42**, 9307 (1990).

³¹ P. Li and F. Ding, *Science Advances* **8**, 10.1126/sci-adv.abq2900 (2022).

³² L. Bignardi, D. Lizzit, H. Bana, E. Travaglia, P. Lacovig, C. E. Sanders, M. Dendzik, M. Michiardi, M. Bianchi, M. Ewert, L. Buß, J. Falta, J. I. Flege, A. Baraldi, R. Larciprete, P. Hofmann, and S. Lizzit, *Physical Review Materials* **3**, 014003 (2019).

³³ F. Matsui, S. Makita, H. Matsuda, T. Ueba, T. Horigome, H. Yamane, K. Tanaka, S. Kera, and N. Kosugi, *e-Journal of Surface Science and Nanotechnology* **18**, 18 (2020).

³⁴ H. Bana, E. Travaglia, L. Bignardi, P. Lacovig, C. E. Sanders, M. Dendzik, M. Michiardi, M. Bianchi, D. Lizzit, F. Presel, D. De Angelis, N. Apostol, P. Kumar Das, J. Fujii, I. Vobornik, R. Larciprete, A. Baraldi, P. Hofmann, and S. Lizzit, *2D Materials* **5**, 035012 (2018).

³⁵ J. H. Jeon, K. H. Chung, H. Kim, and S.-J. Kahng, *Surface Science* **603**, 145 (2009).

³⁶ N. Kawakami, C.-L. Lin, K. Kawahara, M. Kawai, R. Ara-fune, and N. Takagi, *Physical Review B* **96**, 205402 (2017).

³⁷ B. He, G. Tian, J. Gou, B. Liu, K. Shen, Q. Tian, Z. Yu, F. Song, H. Xie, Y. Gao, Y. Lu, K. Wu, L. Chen, and H. Huang, *Surface Science* **679**, 147 (2019).

³⁸ P. Vezzoni Vicente, T. Weiss, D. Meier, W. Zhao, B. S. Tömekçe, M. G. Cuxart, B. P. Klein, D. A. Duncan, T.-L. Lee, A. C. Papageorgiou, M. Muntwiler, A. P. Seitsonen, W. Auwärter, P. Feulner, J. V. Barth, and F. Allegretti, *Physical Review Materials* **8**, 104001 (2024).

³⁹ Y. Lu, W. Xu, M. Zeng, G. Yao, L. Shen, M. Yang, Z. Luo, F. Pan, K. Wu, T. Das, P. He, J. Jiang, J. Martin, Y. P. Feng, H. Lin, and X.-s. Wang, *Nano Letters* **15**, 80 (2014).

⁴⁰ H. Hirayama, *Advances in Physics: X* **6**, 10.1080/23746149.2020.1845975 (2020).

⁴¹ W. E. Morgan, W. J. Stec, and J. R. Van Wazer, *Inorganic Chemistry* **12**, 953 (1973).

⁴² A. Berti, M. D'Alessio, M. Bianchi, L. Bignardi, P. Lacovig, C. Sanders, S. Lizzit, P. Hofmann, A. Marrazzo, and A. Baraldi, *Applied Surface Science* **670**, 160577 (2024).

⁴³ T. Saito, R. Ahmad, F. Kishimoto, T. Higashi, M. Katayama, L. Cavallo, and K. Takanabe, *Journal of Materials Chemistry C* **10**, 17925 (2022).

⁴⁴ M. Jiang, Y. Ding, H. Zhang, J. Ren, J. Li, C. Wan, Y. Hong, M. Qi, B. Mei, L. Deng, Y. Wu, T. Han, H. Zhang, and J. Liu, *Journal of Solid State Electrochemistry* **24**, 2487 (2020).

⁴⁵ J. B. Pendry, *Journal of Physics C: Solid State Physics* **13**, 937 (1980).